# Motional-mode analysis of trapped ions

Henning Kalis,[*] Frederick Hakelberg, Matthias Wittemer, Manuel Mielenz, Ulrich Warring, and Tobias Schaetz[†]

*Albert-Ludwigs-Universität Freiburg, Physikalisches Institut, Hermann-Herder-Straße 3, 79104 Freiburg, Germany*

We present two methods for characterization of motional-mode configurations that are generally applicable to the weak- and strong-binding limit of single or multiple trapped atomic ions. Our methods are essential to realize control of the individual as well as the common motional degrees of freedom. In particular, when implementing scalable radio-frequency trap architectures with decreasing ion-electrode distances, local curvatures of electric potentials need to be measured and adjusted precisely, e.g., to tune phonon tunneling and control effective spin-spin interaction. We demonstrate both methods using single $^{25}$Mg$^+$ ions that are individually confined 40 $\mu$m above a surface-electrode trap array and prepared close to the ground state of motion in three dimensions.

## I. INTRODUCTION

Quantum simulators [1,2] and hybrid quantum systems [3] may present ideal platforms to experimentally explore the emergence and dynamics of complex quantum phenomena, such as many-body physics in strongly correlated systems [2,4] or geometrical frustration [5]. Promising candidates for realizations of scalable quantum simulators, implementing coherent control between constituents, are based on atoms [6], photons [7], electrons [8], or atomic ions [9,10]. Hybrid quantum systems combine two or more different physical constituents, e.g., spins [11], atoms [12], or solid-state devices [13], and pursue studying mutual interactions. Both platforms benefit from advances in microfabrication techniques [14], yielding increasing interaction strengths by decreasing system length scales. Correspondingly, higher-order terms need to be considered, in order to enable precise control of interaction potentials. For example, in microfabricated surface-electrode ion trap arrays [15–17], local potentials, dominated by applied electric trapping potentials define motional modes. For envisioned quantum simulations, motional degrees of freedom can be exploited either within individual sites or between different sites. This, in turn, requires adjustment of motional-mode configurations, i.e., individual orientation of the normal-mode vectors and related motional frequencies, to enable individual tunable intersite interactions [17]. In this work, we introduce and experimentally demonstrate two distinct methods for the analysis of motional-mode configurations that are generally applicable to the weak- and strong-binding limit. For the latter, we cool single ions close to the ground state of motion in three dimensions.

## II. METHODS

To introduce our system, we consider a single ion with charge $Q$ and mass $m$, harmonically bound in three dimensions with motional frequencies $\omega_i$ along normalized mode vectors $\mathbf{u}_i$, where mode $i \in \{1,2,3\}$. Initially, modes are arbitrarily rotated with respect to the axes of the laboratory frame,

labeled $x$, $y$, and $z$, and we parametrize mode orientations by three subsequent rotations around these spatially fixed axes by the angles $\phi_x$, $\phi_y$, and $\phi_z$, with the corresponding composite rotation matrix $\mathcal{R}(\phi_x,\phi_y,\phi_z)$. Further, motional states are described by Fock state distributions $\mathcal{P}_i(n_i)$, where $n_i$ are the corresponding phonon numbers of mode $i$. We consider one electronic ground state $|g_\lambda\rangle$ and one excited state $|e_\lambda\rangle$ with energy difference $\hbar\omega_\lambda \gg \hbar\omega_i$ and a natural linewidth $\Gamma_\lambda$, with $\lambda \in \{w,s\}$. For $\Gamma_w \gg \omega_i$, the so called weak-binding limit, our first method is suited best to determine $\boldsymbol{\omega}/(2\pi) \equiv \{\omega_1,\omega_2,\omega_3\}/(2\pi)$ and $\{\phi_x,\phi_y,\phi_z\}$. In Fig. 1(a) we show a simplified illustration for $\{\phi_x,\phi_y,\phi_z\} \approx \{0,0,35\}^\circ$. The method is based on the excitation of the modes by an electric field $\mathbf{E}_{exc}$ oscillating at $\omega_{exc} \approx \omega_i$ for duration $t_{exc}$. Motional amplitudes $A_i(t_{exc}) \propto \langle \mathbf{u}_i,\mathbf{E}_{exc}\rangle$ along $\mathbf{u}_i$ can be evaluated classically, when excited to a coherent state with $\langle n_i \rangle \equiv \langle \mathcal{P}_i(n_i)\rangle \gg 0$. Subsequently, the fluorescence rate $\Omega_F$ induced by a laser tuned to $\omega_w$ with wave vector $\mathbf{k}_w$ and rate $\Omega_w < \Omega_F$ [see Fig. 1(a)] is modulated as a function of $A_i\langle \mathbf{u}_i,\mathbf{k}_w\rangle$ due to the Doppler effect [18]. In the following, we refer to a normalized fluorescence $\mathcal{F} \equiv \Omega_F/\Omega'_F$, where $\Omega'_F$ represents the unmodulated rate. In contrast, in the strong-binding limit, $\Gamma_s \ll \omega_i$, we present our second method to determine mode configurations; we sketch the corresponding example in Fig. 1(b). Here, motional excitation of single quanta is performed via a laser, exemplarily tuned to $\omega_s + \omega_1$, coherently coupling the electronic and motional states at a rate $\Omega_s \propto \langle e_s,1,0,0|e^{i\langle \mathbf{k}_s,\mathbf{u}_1\rangle}|g_s,0,0,0\rangle$ [19]. We determine the angle between $\mathbf{k}_s$ and $\mathbf{u}_i$ by evaluating $\Omega_s$ for excitation at $\omega_s + \omega_i$, which is efficiently performed when $\eta_i\sqrt{2\langle n_i\rangle + 1} \ll 1$, with the Lamb-Dicke parameter $\eta_i = |\langle \mathbf{k}_s,\mathbf{u}_i\rangle|\sqrt{\hbar/(2m\omega_i)}$. Application of either method yields unique results for arbitrary mode configurations, when sequentially probed from multiple directions.

## III. EXPERIMENTS

We experimentally demonstrate both methods with single $^{25}$Mg$^+$ ions harmonically confined in a surface-electrode trap array fabricated by Sandia National Laboratories [17,20]. The array inherits a triangular arrangement of individual traps with an intersite distance of $d \approx 40$ $\mu$m (see Fig. 2). Three-dimensional confinement at three distinct trapping sites is realized by a radio-frequency (rf) potential $\phi_{rf}(\mathbf{r})$, oscillating at

---

*henning.kalis@physik.uni-freiburg.de
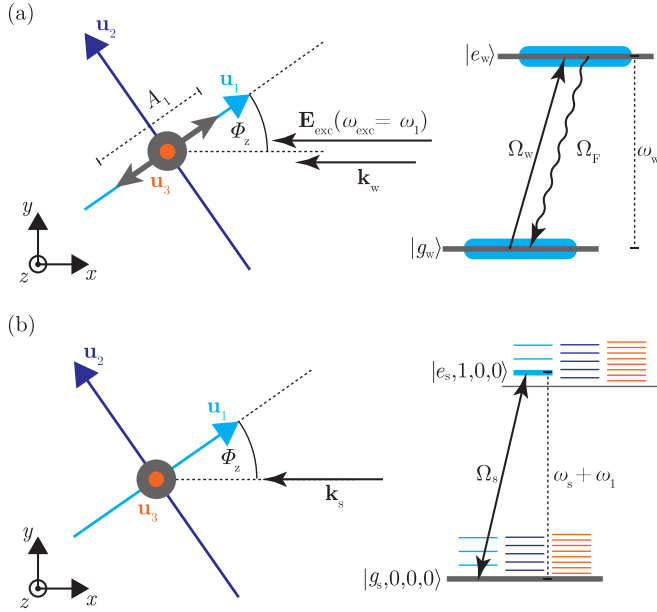†tobias.schaetz@physik.uni-freiburg.de

FIG. 1. Illustration of both mode-analysis methods applicable to the weak- and strong-binding limit. In our simplified example, the motional modes are rotated relative to the coordinate system by $\phi_z$. (a) In the weak-binding limit, the mode $\mathbf{u}_1$ is resonantly excited by an electric field $\mathbf{E}_{\text{exc}}$ oscillating at $\omega_{\text{exc}} = \omega_1$ to motional amplitude $A_1 \propto \langle \mathbf{u}_1, \mathbf{E}_{\text{exc}} \rangle$ with $\langle n_1 \rangle \gg 0$. Subsequently, a laser with wave vector $\mathbf{k}_{\text{w}}$ along $x$ resonantly drives the transition $|g_{\text{w}}\rangle \leftrightarrow |e_{\text{w}}\rangle$. Blue bars illustrate the natural linewidth $\Gamma_{\text{w}}$. In turn, the mode orientation is derived considering the Doppler effect and the related decrease of the fluorescence rate $\Omega_{\text{F}}$ as a function of $A_1 \langle \mathbf{u}_1, \mathbf{k}_{\text{w}} \rangle$. (b) In the strong-binding limit, a laser is tuned to $\omega_{\text{s}} + \omega_1$ with wave vector $\mathbf{k}_{\text{s}}$ along $x$, coherently coupling the electronic (gray bars) and motional states (colored bars), e.g., $|g_{\text{s}}, 0, 0, 0\rangle$ to $|e_{\text{s}}, 1, 0, 0\rangle$. Here, the coupling rate $\Omega_{\text{s}} \propto \langle e_{\text{s}}, 1, 0, 0 | e^{i\langle \mathbf{k}_{\text{s}}, \mathbf{u}_1 \rangle} | g_{\text{s}}, 0, 0, 0 \rangle$ encodes the mode configuration.
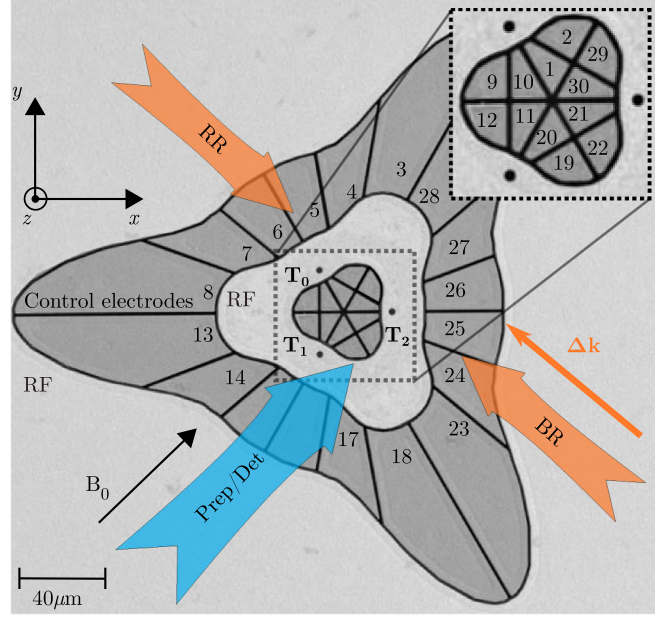


FIG. 2. Illustration of the setup showing a false colored scanning electron microscope image of our trap. The array consists of two radio-frequency electrodes (light gray) and 30 control electrodes (dark gray), labeled $1 \ldots 30$. Trapping sites are denoted $\mathbf{T}_j$ with $j \in \{0, 1, 2\}$ and are separated by $\approx 40\,\mu\text{m}$; here, all experiments are carried out with single $^{25}\text{Mg}^+$ ions trapped near $\mathbf{T}_2$. Motional excitation fields $\mathbf{E}_{\text{exc}} = U_{\text{exc}}\mathbf{E}_l$ oscillating at $\omega_{\text{exc}}$ are applied via the $l$th control electrode. A set of laser beams, propagating along $\mathbf{k}_{\text{w}}$ and parallel to the magnetic field $|\mathbf{B}_0| \approx 4.65\,\text{mT}$, is used for preparation and detection of the electronic degrees of freedom (blue arrow). Two more beams, labeled BR/RR (red arrows), with an effective wave vector $\Delta\mathbf{k} \equiv \mathbf{k}_{\text{s}}$, are implemented to coherently couple electronic and motional states via two-photon stimulated Raman transitions.

$\Omega_{\text{rf}}/(2\pi) = 88.1\,\text{MHz}$ with a peak voltage $U_{\text{rf}} \approx 90\,\text{V}$ applied in phase to two rf electrodes. We refer to the trapping sites as $\mathbf{T}_j$ with $j \in \{0, 1, 2\}$ and, e.g., we estimate $\mathbf{T}_2 \approx \{23, 0, 36\}\,\mu\text{m}$ for our experimental parameters. Typical motional frequencies are $\boldsymbol{\omega}/(2\pi) \approx \{3.6, 4.8, 5.9\}\,\text{MHz}$. Our array provides 30 control electrodes that we offset to a constant voltage $\in [-10, 10]\,\text{V}$ to control the motional degrees of freedom [17]. The $l$th electrode biased at 1 V generates a potential $\phi_l(\mathbf{r})$ with $l \in \{1, \ldots, 30\}$, which is evaluated, e.g., at $\mathbf{r} = \mathbf{T}_2$, using the gapless-plane approximation [21]. For the $l$th electrode of choice we can create oscillating $\phi_l(\mathbf{r})$ by applying a signal from a direct digital synthesizer (DDS) at $\omega_{\text{exc}}/(2\pi) \approx 1$–$10\,\text{MHz}$ and peak voltages $U_{\text{exc}} \approx 0.1$–$1\,\text{mV}$.

For preparation, manipulation, and detection of the electronic and motional states we employ laser beams with wavelengths close to $280\,\text{nm}$ [22]. All beams propagate parallel to the surface ($xy$ plane). Four overlapping $\sigma^+$-polarized beams, propagating parallel to a static magnetic field $|\mathbf{B}_0| \approx 4.65\,\text{mT}$, are used for Doppler cooling and electronic-state preparation. One beam (BDD) is detuned by $\Delta_{\text{BDD}}/(2\pi) \approx -8\Gamma_{\text{w}}/(2\pi)$ from the cycling transition $|g\rangle \equiv |g_{\{\text{w},\text{s}\}}\rangle = |S_{1/2}, F = 3, m_F = +3\rangle \leftrightarrow |e_{\text{w}}\rangle \equiv |P_{3/2}, F = 4, m_F = +4\rangle$ with a natural linewidth of

$\Gamma_{\text{w}}/(2\pi) \approx 42\,\text{MHz}$. The other beam (BD) with wave vector $\mathbf{k}_{\text{BD}} \equiv \mathbf{k}_{\text{w}}$ is detuned by $\Delta_{\text{BD}}/(2\pi) \approx -\Gamma_{\text{w}}/(4\pi)$ with intensity $I_{\text{BD}} \approx I_{\text{sat}}/2$, where $I_{\text{sat}} \approx 2500\,\text{W/m}^2$ denotes the saturation intensity; for state-dependent fluorescence detection [19], we switch $\Delta_{\text{BD}}/(2\pi) \approx -5\,\text{MHz}$. Further, two optical-pumping beams are used to prepare $|g\rangle$. We implement two more beams (BR/RR) with an effective wave vector $\Delta\mathbf{k} \equiv \mathbf{k}_{\text{s}}$ along $\{-1/\sqrt{2}, 1/\sqrt{2}, 0\}$ to drive two-photon stimulated Raman transitions [19], with $\Gamma_{\text{s}} \ll \Omega_{\text{s}} \ll \omega_{\text{s}}$, between $|g\rangle$ and $|e_{\text{s}}\rangle \equiv |S_{1/2}, F = 2, m_F = +2\rangle$, separated by $\omega_{\text{s}}/(2\pi) \approx 1681.5\,\text{MHz}$. The beams are polarized $1/\sqrt{2}(\sigma^+ + \sigma^-)$ and $\pi$, respectively, coupling $|g\rangle$ and $|e_{\text{s}}\rangle$ via a common virtual level, detuned by $\Delta_{\text{R}}/(2\pi) \approx 33\,\text{GHz}$ from the $P_{3/2}$ manifold. The relative detuning of the beams can be varied between $\omega_{\text{R}}/(2\pi) \approx \omega_{\text{s}}/(2\pi) \pm 40\,\text{MHz}$.

### A. Weak-binding limit

To demonstrate the first method we apply the experimental sequence, illustrated in Fig. 3(a), to a single ion trapped near $\mathbf{T}_2$: After Doppler cooling and preparation of $|g\rangle$, the DDS signal at $\omega_{\text{exc}}$ is capacitively coupled onto one preselected control electrode for duration $t_{\text{exc}} = 10\,\mu\text{s}$. Finally, we detect the fluorescence on the transition $|g\rangle \leftrightarrow |e_{\text{w}}\rangle$ for a duration of $100\,\mu\text{s}$.
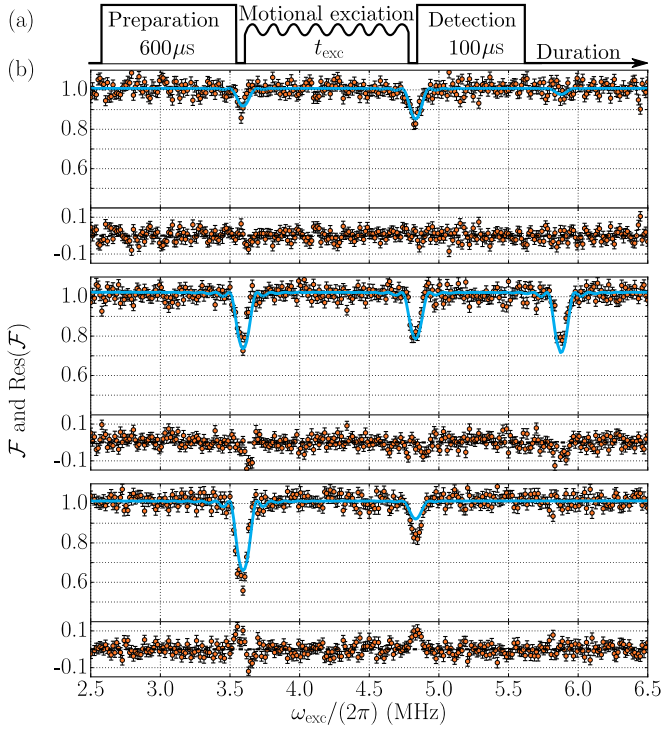
FIG. 3. Determination of mode configurations, i.e., motional frequencies and mode orientations, in the weak-binding limit. (a) Experimental sequences (not to scale; durations between subsequent operations remain $<500$ ns) performed with a single ion trapped near $\mathbf{T}_2$, beginning with Doppler cooling and preparation of $|g\rangle$, followed by a motional excitation pulse of duration $t_{\text{exc}} = 10\,\mu s$, and finalized by the measurement of $\Omega_{\text{F}}$, revealing the normalized fluorescence $\mathcal{F}$. (b) Excitation pulses are applied using $\mathbf{E}_{\text{exc}} \propto \mathbf{E}_l$, representatively shown for $l \in \{22,26,28\}$ (from top to bottom), with corresponding $\mathcal{F}$ as a function of the excitation frequency $\omega_{\text{exc}}$. Data points are taken in random order and averaged over 200 repetitions of sequences with fixed parameter settings, where error bars denote the statistic uncertainties. A combined model fit (solid lines) considering ten different electrodes $l \in \{21\ldots30\}$ yields mode configurations: $\{\phi_x,\phi_y,\phi_z\} = \{-4(1)_{\text{stat}}(2)_{\text{sys}}, -36(1)_{\text{stat}}(4)_{\text{sys}}, -3(1)_{\text{stat}}(1)_{\text{sys}}\}^\circ$ and $\boldsymbol{\omega}/(2\pi) = \{3.584(2)_{\text{stat}},4.833(3)_{\text{stat}},5.878(4)_{\text{stat}}\}$ MHz. Residuals are shown below each spectrum.

In subsequent measurements, we choose the ten electrodes $l \in \{21\ldots30\}$ with $\mathbf{E}_{\text{exc}} = U_{\text{exc}}\mathbf{E}_l \equiv -U_{\text{exc}}\nabla\phi_l(\mathbf{r})|_{\mathbf{r}=\mathbf{T}_2}$, record $\mathcal{F}$ as a function of $\omega_{\text{exc}}$, subtract the independently determined stray-light contributions from the total photon counts, and average each data point over 200 repetitions. In Fig. 3(b), we representatively show recorded $\mathcal{F}$ for selected electrodes $l \in \{22,26,28\}$. We find that the full widths at half maximum of recorded resonances are given by $1/t_{\text{exc}} \approx 100$ kHz.

For the analysis, we consider that the motional modes $\mathbf{u}_i$ remain uncoupled and introduce a model for the modulation of $\mathcal{F}$, based on the classical driven harmonic oscillator (see Appendix A for details). Here, final motional amplitudes are given by

$$A_i(t_{\text{exc}}) = \frac{Q}{m}U_{\text{exc}}|\langle\mathbf{u}_i,\mathbf{E}_l\rangle|\frac{2}{\omega_{\text{exc}}^2 - \omega_i^2}\sin\left[\frac{t_{\text{exc}}}{2}(\omega_{\text{exc}} - \omega_i)\right],$$
$$(1)$$

where we assume that the ion is initially at the center of the harmonic potential and at rest. Further, motional excitations result in [23]

$$\mathcal{F} = \left(\frac{\Gamma_{\text{w}}}{2}\right)^2 \prod_{i=1}^{3}\sum_{v=-\infty}^{\infty}\frac{J_v(\beta_i)^2}{(\Delta_{\text{BD}} + v\,\omega_i)^2 + (\Gamma_{\text{w}}/2)^2}, \quad (2)$$

where we use the $v$th Bessel function $J_v$ and the modulation index $\beta_i = |\langle\mathbf{u}_i,\mathbf{k}_{\text{BD}}\rangle|A_i(t_{\text{exc}})$. In a combined fit of this model to all ten spectra, with seven free parameters, we obtain $\{\phi_x,\phi_y,\phi_z\} = \{-4(1)_{\text{stat}}(2)_{\text{sys}}, -36(1)_{\text{stat}}(4)_{\text{sys}}, -2(1)_{\text{stat}}(1)_{\text{sys}}\}^\circ$, $U_{\text{exc}} = 731(8)_{\text{stat}}\,\mu V$, and $\boldsymbol{\omega}/(2\pi) = \{3.584(2)_{\text{stat}},4.833(3)_{\text{stat}},5.878(4)_{\text{stat}}\}$ MHz, where we truncate the sum in Eq. (2) at $|v| = 15$. The mode configuration is uniquely determined by the fit and from the parameters we calculate the (quasistatic) curvature of the total trapping potential near $\mathbf{T}_2$:

$$H_T = \frac{m}{Q}\mathcal{R}(\phi_x,\phi_y,\phi_z)(\boldsymbol{\omega}\mathbb{1}\,\boldsymbol{\omega}^T)\mathcal{R}(\phi_x,\phi_y,\phi_z)^T$$

$$= \begin{pmatrix} 277(16) & -14(20) & -53(7) \\ -14(20) & 133(5) & 14(20) \\ -53(7) & 14(20) & 313(17) \end{pmatrix}\mu V/(\mu m)^2. \quad (3)$$

Here, $\mathbb{1}$ denotes the three-dimensional identity matrix and uncertainties correspond to systematic uncertainties of the angles. In contrast, statistical uncertainties of fitted motional frequencies result in less than 1% relative uncertainties in entries of $H_T$. The dominating systematic uncertainty in the mode configuration is caused by the uncertainty of the ion position $\Delta\mathbf{T}_2 = \pm(1,1,5)\,\mu m$ and a related uncertainty in $\mathbf{E}_l$. Due to differential capacities of electrodes smaller than 3 fF, compared to filter capacitors of several hundreds of pF, we consider $U_{\text{exc}}$ to be equal for all electrodes. Typical motional amplitudes after resonant excitation amount to $|A_i| \approx 500$ nm, corresponding to a coherent state with $\langle n_i\rangle \approx 1000$, while we calculate initial thermal states $\{\langle n_1\rangle,\langle n_2\rangle,\langle n_3\rangle\} \approx \{7,9,16\}$, assuming optimal Doppler cooling [19].

### B. Strong-binding limit

Since mode configurations are subject to day-to-day variations of experimental parameters, e.g., due to stray potentials, we exploit our first method to perform a reference measurement and obtain $\{\phi_x,\phi_y,\phi_z\} = \{1(3)_{\text{stat}}(5)_{\text{sys}}, -50(2)_{\text{stat}}(5)_{\text{sys}}, -13(2)_{\text{stat}}(4)_{\text{sys}}\}^\circ$. Using this dataset also for comparison, we apply our second method, using the same ion near $\mathbf{T}_2$ to avoid changes caused by intermittent loading, to determine the mode orientation by the following experimental sequence [see Fig. 4(a)]: After preparation of $|g\rangle$, we use resolved sideband cooling [24] to prepare all motional states close to their ground states. Then we couple the electronic and motional states with BR/RR along $\Delta\mathbf{k}$ for variable pulse duration $t_{\text{pulse}}$, and derive the final population $P_{|g\rangle}$. We set $\boldsymbol{\omega}/(2\pi) = \{3.76,4.54,5.76\}$ MHz, determined by calibration measurements, and in subsequent experiments we probe different couplings at $\omega_{\text{R}} \approx \{\omega_s,\omega_s + \omega_1,\omega_s + \omega_2,\omega_s + \omega_3\}$. We show corresponding results of $P_{|g\rangle}$ as a function of $t_{\text{pulse}}$ in
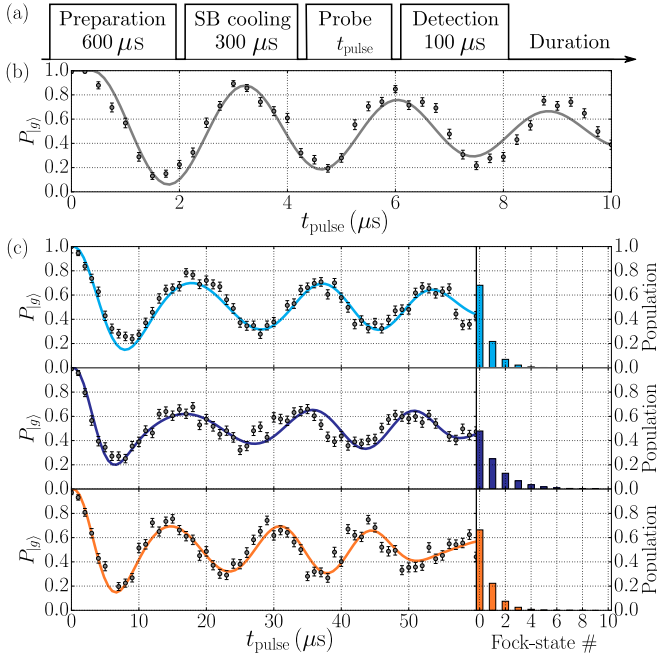
FIG. 4. Determination of mode orientations in the strong-binding limit. (a) After Doppler cooling and preparation of $|g\rangle$ and $\langle n_i \rangle \leqslant 1$ via resolved sideband cooling, we apply a coherent coupling of electronic and motional states with lasers BR and RR tuned to $\omega_R$ for duration $t_{\text{pulse}}$ and derive $P_{|g\rangle}$, the probability of detecting the ion in $|g\rangle$. Here, $\boldsymbol{\omega}$ is determined by calibration measurements (not to scale; durations between subsequent operations remain $<500$ ns). In subsequent measurements, we record $P_{|g\rangle}$ as a function of $t_{\text{pulse}}$ for different couplings, where $\omega_R \approx \omega_s$ [see (b)] and $\omega_R \approx \{\omega_s + \omega_1, \omega_s + \omega_2, \omega_s + \omega_3\}$ [see (c)]. A combined model fit to the data (solid lines) and results from complementary measurements yield $\{\phi_x, \phi_y, \phi_z\} = \{-9(2)_{\text{stat}}(5)_{\text{sys}}, -51(2)_{\text{stat}}(5)_{\text{sys}}, -15(1)_{\text{stat}}(5)_{\text{sys}}\}^\circ$, $\{\langle n_1 \rangle, \langle n_2 \rangle, \langle n_3 \rangle\} = \{0.5(1)_{\text{stat}}, 1.0(1)_{\text{stat}}, 0.44(5)_{\text{stat}}\}$. Corresponding calculated thermal distributions $\mathcal{P}_i(n_i)$ of each mode are shown in bar charts on the right.

Fig. 4(b). For the analysis of our data, we use

$$P_{|g\rangle}(t) = \sum_{n_i=0}^{n_{i,\max}} \left[ \prod_{i=1}^{3} \mathcal{P}_i(n_i) \right] \cos^2 \left( \frac{\Omega_s}{2} t \right), \quad (4)$$

where the motional-sensitive Rabi rate is given by

$$\Omega_s = \langle e_s, n_1', n_2', n_3' | e^{i \langle \Delta \mathbf{k}, \mathbf{u}_i \rangle} | g, n_1, n_2, n_3 \rangle$$

$$\approx \Omega_0 \prod_{i=1}^{3} \exp \left( \frac{-\eta_i^2}{2} \right) \eta_i^{|\Delta n_i|} \sqrt{\frac{n_{i<}!}{n_{i>}!}} L_{n_{i<}}^{|\Delta n_i|} (\eta_i^2). \quad (5)$$

Here, $n_{i<}$ ($n_{i>}$) is the lesser (greater) of $n_i' = n_i + \Delta n_i$ and $n_i$, while $\Delta n_i$ denotes the change in the phonon number, i.e., the order of the sideband transition. Further, $L_{n_{i<}}^{|\Delta n_i|}$ is the generalized Laguerre polynomial and $\Omega_0$ is the motional-independent Rabi rate [19], tuned by beam parameters of BR and RR. Note, since we currently probe along $\Delta \mathbf{k}$ only, mode orientations are not uniquely determined and two out of three angles are derived. Therefore, we iteratively fix one of the angles in combined fits to all datasets using our reference measurements and average the outcomes.

For the analysis, we add a term in Eq. (4) to account for a decoherence rate $\Gamma_{\text{dec}}$, truncate the sum in Eq. (4) at $n_{i,\max} = 11$, and assume thermal distributions of $\mathcal{P}_i(n_i)$. We find $\{\phi_x, \phi_y, \phi_z\} = \{-9(2)_{\text{stat}}(5)_{\text{sys}}, -51(2)_{\text{stat}}(5)_{\text{sys}}, -15(1)_{\text{stat}}(5)_{\text{sys}}\}^\circ, \{\langle n_1 \rangle, \langle n_2 \rangle, \langle n_3 \rangle\} = \{0.5(1)_{\text{stat}}, 1.0(1)_{\text{stat}}, 0.44(5)_{\text{stat}}\}, \Omega_0/(2\pi) = 390(3)_{\text{stat}}$ kHz, and $\Gamma_{\text{dec}}/(2\pi) = 13(3)_{\text{stat}}$ kHz. Here, the systematic uncertainty is dominated by the limited knowledge of the orientation of $\Delta \mathbf{k}$ by $\pm 5^\circ$.

## IV. CONCLUSION

To summarize, we introduce two general methods to fully characterize mode configurations of single ions. To allow for detection of arbitrary mode configurations, each method needs to be applied from multiple different directions or can be supplemented by each other. In general, probing along an increasing number of directions can yield decreasing uncertainties of determined mode orientations (see Appendix B). Since motional-mode configurations may be subject to time-dependent experimental parameters, which vary from ion to ion, due to charging effects, e.g., caused by the photoionization laser, it is desirable having such methodologies at hand to frequently and efficiently perform a mode analysis. Further, our methods can be readily extended to characterization of mode configurations of multiple ions. They may serve as standard procedures in experiments, where precise control of motional modes is inevitable, e.g., in two-dimensional ion trap arrays, used for quantum simulations [10,17,25]. In this context, tuning the motional parameters permits state preparation of sympathetically cooled ions at all sites simultaneously as well as setting intersite Coulomb interactions. The latter has been demonstrated to mediate an effective interaction, that depends on the electronic states of the constituents and can be used either as spin-spin interaction or as data bus between qubits [9,25–28]. In addition, it may directly enable simulation of bosonic particles via phonon tunneling between neighboring sites defined by the ions, while corresponding local mode configurations define tunneling rates, pathways, and related phases [29]. To establish a necessary level of control, systematic uncertainties need to be improved. Moreover, adjusting mode configurations can aid either exploiting a more robust interaction bus [30] or investigating the sources of anomalous heating [31], since recent experiments found a dependency of heating rates on the orientation of motional-mode vectors relative to the electrode structures [32]. Further, our methods may be deployed to benchmark application of appropriate control potentials up to second order and, therefore, to compensate stray curvatures [17]. In particular, in experiments with optical ion traps [33] or Rydberg states of ions [34], precise adjustment of curvatures is necessary, maximizing trapping efficiencies and durations.

## APPENDIX A: MODULATION AMPLITUDE IN A CLASSICAL DRIVEN HARMONIC OSCILLATOR

Let us describe the dynamics of the single trapped ion at position $u(t)$ with charge $Q$, mass $m$, and eigenfrequency $\omega$ that is excited by an electric field $E_{\text{exc}}$, oscillating at $\omega_{\text{exc}}$, with a classical driven harmonic oscillator. Neglecting intermode couplings we consider the model to be one dimensional, omitting mode indices:

$$\frac{\partial^2}{\partial t^2} u(t) + \omega^2 u(t) - \frac{Q E_{\text{exc}}}{m} \sin(\omega_{\text{exc}} t) = 0. \quad (A1)$$

Considering initial conditions $v(t) \equiv \partial u(t)/\partial t|_{t=0} = 0$ and $u(0) = 0$ the solution reads

$$u(t) = \frac{Q E_{\text{exc}}}{m\omega} \frac{\omega_{\text{exc}} \sin(\omega t) - \omega \sin(\omega_{\text{exc}} t)}{(\omega_{\text{exc}}^2 - \omega^2)}. \quad (A2)$$

Further, the motional amplitude of the ion $|A(t_{\text{exc}})|$ after excitation for duration $t_{\text{exc}}$ reads

$$
\begin{aligned}
|A(t_{\text{exc}})| &= \frac{u(t_{\text{exc}})}{\sin\{\arctan[\omega u(t_{\text{exc}})/v(t_{\text{exc}})]\}} \\
&= \frac{Q E_{\text{exc}}}{m} \left| \frac{1}{\omega^2 - \omega_{\text{exc}}^2} \right| \left( \left(1 + \frac{\omega^2}{\omega_{\text{exc}}^2} \right. \right. \\
&\quad + \left[1 - \frac{\omega^2}{\omega_{\text{exc}}^2}\right] \cos^2[\omega_{\text{exc}} t_{\text{exc}}] \\
&\quad - \left[1 + \frac{\omega^2}{\omega_{\text{exc}}^2}\right] \cos[\{\omega - \omega_{\text{exc}}\} t_{\text{exc}}] \\
&\quad \left. \left. + \left[\frac{\omega}{\omega_{\text{exc}}} - 1\right] \cos[\{\omega + \omega_{\text{exc}}\} t_{\text{exc}}] \right)^{\frac{1}{2}} \right. \\
&\approx \frac{2 Q E_{\text{exc}}}{m} \left| \frac{\sin\left([\omega_{\text{exc}} - \omega]\frac{t_{\text{exc}}}{2}\right)}{\omega_{\text{exc}}^2 - \omega^2} \right|. \quad (A3)
\end{aligned}
$$

In the last step we used the fact that in typical experiments the excitation frequency is always on the same order of magnitude as the eigenfrequency of the ion $\omega \approx \omega_{\text{exc}}$, keeping only slowly oscillating terms. In the resonant case $\omega_{\text{exc}} \rightarrow \omega$ the amplitude is given by

$$A_{\text{res}}(t_{\text{exc}}) = \frac{Q E_{\text{exc}} t_{\text{exc}}}{2 m \omega_{\text{exc}}} \quad (A4)$$

using L'Hôpital's rule.

## APPENDIX B: UNCERTAINTIES OF OBTAINED MODE ORIENTATIONS IN THE WEAK-BINDING LIMIT

The result presented in Eq. (3) is based on the combined analysis of ten fluorescence spectra. Here, we vary the number of spectra, i.e., number of electrodes $\mathcal{N}_{\text{el}}$, used for the analysis and study obtained mode angles and corresponding uncertainties. For $\mathcal{N}_{\text{el}} \in \{1,2,\ldots,9\}$ we perform $\mathcal{N}_{\text{fit}}$ fits for all possible combinations of electrodes $l \in \{21 \ldots 30\}$; we show $\mathcal{N}_{\text{fit}}$ in Fig. 5(a). For all fits we keep the angles $\{\phi_x, \phi_y, \phi_z\}$ and the peak voltage $U_{\text{exc}}$ as free parameters, while setting frequencies to $\boldsymbol{\omega}/(2\pi) = \{3.584, 4.833, 5.878\}$ MHz. In Fig. 5(b)
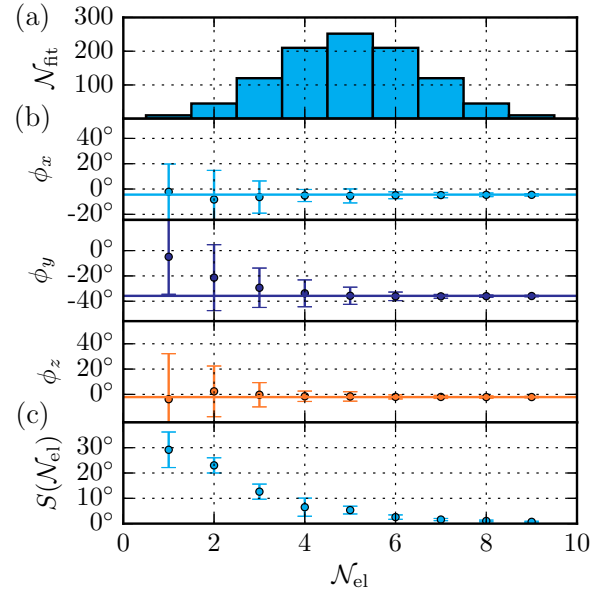


FIG. 5. Evolution of statistical uncertainties in dependence of the number of electrodes $\mathcal{N}_{\text{el}}$. (a) Number of fits $\mathcal{N}_{\text{fit}}$ that have to be performed for all possible combinations of electrodes. (b) Mean angles $\langle \phi_\alpha \rangle$ averaged over all combinations, where error bars are given by $\sigma_\alpha$. Horizontal lines represent the result obtained for $\mathcal{N}_{\text{el}} = 10$. (c) Evolution of $S(\mathcal{N}_{\text{el}})$, where $S(5) \approx 4°$ yields values comparable to the maximum estimated systematic uncertainty for this dataset.

we present the means of the resulting angles (data points)

$$\langle \phi_\alpha \rangle = \frac{1}{\mathcal{N}_{\text{fit}}} \sum_{d=1}^{\mathcal{N}_{\text{fit}}} \phi_\alpha^d \quad (B1)$$

and their corresponding sample standard deviation (error bars)

$$\sigma_\alpha = \sqrt{\frac{1}{\mathcal{N}_{\text{fit}} - 1} \sum_{d=1}^{\mathcal{N}_{\text{fit}}} \left(\phi_\alpha^d - \langle \phi_i \rangle\right)^2}. \quad (B2)$$

To judge the significance of a certain combination of fixed $\mathcal{N}_{\text{el}}$ we give the mean $\sigma_\alpha$

$$S(\mathcal{N}_{\text{el}}) \equiv \frac{1}{3} \sum_{\alpha=x,y,z} \sigma_\alpha \quad (B3)$$

in Fig. 5(c).

In general, the outcome of such analysis strongly depends on the geometry of the used trap electrodes and on the mode orientations. Also for traps, featuring a few control electrodes only, our method can yield unique mode orientations with smaller uncertainties than presented for our case. For example, in a common case for many conventional ion trap designs, at least one mode vector is pointing along a certain direction, e.g., $\mathbf{u}_3 \parallel z$ as illustrated in Fig. 1(a). Here, we assume for simplicity that $\mathbf{E}_{\text{exc}}$ (from a single electrode) and $\mathbf{k}_{\text{det}}$ are parallel and lie in the $xy$ plane, such that the modulation indices $\beta_i$ for modes $i = \{1,2\}$ can be determined. As a consequence, we find that $\beta_1 \neq \beta_2$ for $\phi_z \neq 45°$, enabling a unique mode analysis with a single probing direction only.

[1] R. P. Feynman, Int. J. Theor. Phys. **21**, 467 (1982); I. Buluta and F. Nori, Science **326**, 108 (2009); T. Schaetz, C. R. Monroe, and T. Esslinger, New J. Phys. **15**, 085009 (2013); I. Georgescu, S. Ashhab, and F. Nori, Rev. Mod. Phys. **86**, 153 (2014).

[2] J. I. Cirac and P. Zoller, Nat. Phys. **8**, 264 (2012).

[3] Z.-L. Xiang, S. Ashhab, J. Q. You, and F. Nori, Rev. Mod. Phys. **85**, 623 (2013).

[4] K. Eckert, O. Romero-Isart, M. Rodriguez, M. Lewenstein, E. S. Polzik, and A. Sanpera, Nat. Phys. **4**, 50 (2008).

[5] R. Moessner, S. L. Sondhi, and P. Chandra, Phys. Rev. Lett. **84**, 4457 (2000).

[6] M. Lewenstein, A. Sanpera, V. Ahufinger, B. Damski, A. Sen De, and U. Sen, Adv. Phys. **56**, 243 (2007).

[7] M. J. Hartmann, F. G. S. L. Brandão, and M. B. Plenio, Nat. Phys. **2**, 849 (2006).

[8] R. Hanson and D. D. Awschalom, Nature (London) **453**, 1043 (2008).

[9] D. Porras and J. I. Cirac, Phys. Rev. Lett. **96**, 250501 (2006).

[10] C. Schneider, D. Porras, and T. Schaetz, Rep. Prog. Phys. **75**, 024401 (2012).

[11] K. C. Nowack, F. H. L. Koppens, Y. V. Nazarov, and L. M. K. Vandersypen, Science **318**, 1430 (2007).

[12] M. Saffman, T. G. Walker, and K. Mølmer, Rev. Mod. Phys. **82**, 2313 (2010); Z. J. Deng, Q. Xie, C. W. Wu, and W. L. Yang, Phys. Rev. A **82**, 034306 (2010).

[13] E. Togan, Y. Chu, A. S. Trifonov, L. Jiang, J. Maze, L. Childress, M. V. G. Dutt, A. S. Sørensen, P. R. Hemmer, A. S. Zibrov, and M. D. Lukin, Nature (London) **466**, 730 (2010).

[14] N. Daniilidis, S. Narayanan, S. A. Möller, R. Clark, T. E. Lee, P. J. Leek, A. Wallraff, S. Schulz, F. Schmidt-Kaler, and H. Häffner, New J. Phys. **13**, 013032 (2011); R. C. Sterling, H. Rattanasonti, S. Weidt, K. Lake, P. Srinivasan, S. C. Webster, M. Kraft, and W. K. Hensinger, Nat. Comm. **5**, 3637 (2014).

[15] S. Seidelin, J. Chiaverini, R. Reichle, J. J. Bollinger, D. Leibfried, J. Britton, J. H. Wesenberg, R. B. Blakestad, R. J. Epstein, D. B. Hume, W. M. Itano, J. D. Jost, C. Langer, R. Ozeri, N. Shiga, and D. J. Wineland, Phys. Rev. Lett. **96**, 253003 (2006).

[16] R. Schmied, J. H. Wesenberg, and D. Leibfried, Phys. Rev. Lett. **102**, 233002 (2009).

[17] M. Mielenz, H. Kalis, M. Wittemer, F. Hakelberg, U. Warring, R. Schmied, M. Blain, P. Maunz, D. L. Moehring, D. Leibfried, and T. Schaetz, Nat. Comm. **7**, 11839 (2016).

[18] S. R. Jefferts, C. Monroe, E. W. Bell, and D. J. Wineland, Phys. Rev. A **51**, 3112 (1995); T. Gudjons, P. Seibert, and G. Werth, App. Phys. B **65**, 57 (1997).

[19] D. Leibfried, R. Blatt, C. Monroe, and D. Wineland, Rev. Mod. Phys. **75**, 281 (2003).

[20] B. Tabakov, F. Benito, M. Blain, C. R. Clark, S. Clark, R. A. Haltli, P. Maunz, J. D. Sterk, C. Tigges, and D. Stick, Phys. Rev. App. **4**, 031001 (2015).

[21] D. Hucul, M. Yeo, S. Olmschenk, C. Monroe, W. K. Hensinger, and J. Rabchuk, Journal of Quantum Information and Computation **8**, 501 (2008); J. H. Wesenberg, Phys. Rev. A **78**, 063410 (2008); R. Schmied, New J. Phys. **12**, 023038 (2010).

[22] A. Friedenauer, F. Markert, H. Schmitz, L. Petersen, S. Kahra, M. Herrmann, T. Udem, T. W. Hänsch, and T. Schätz, App. Phys. B **84**, 371 (2006).

[23] R. G. DeVoe, J. Hoffnagle, and R. G. Brewer, Phys. Rev. A **39**, 4362 (1989); D. J. Berkeland, J. D. Miller, J. C. Bergquist, W. M. Itano, and D. J. Wineland, J. App. Phys. **83**, 5025 (1998).

[24] F. Diedrich, J. C. Bergquist, W. M. Itano, and D. J. Wineland, Phys. Rev. Lett. **62**, 403 (1989).

[25] A. C. Wilson, Y. Colombe, K. R. Brown, E. Knill, D. Leibfried, and D. J. Wineland, Nature (London) **512**, 57 (2014).

[26] D. Leibfried, B. DeMarco, V. Meyer, D. Lucas, M. Barrett, J. Britton, W. M. Itano, B. Jelenković, C. Langer, T. Rosenband, and D. J. Wineland, Nature (London) **422**, 412 (2003).

[27] A. Friedenauer, H. Schmitz, J. T. Glueckert, D. Porras, and T. Schaetz, Nat. Phys. **4**, 757 (2008).

[28] M. Harlander, R. Lechner, M. Brownnutt, R. Blatt, and W. Hänsel, Nature (London) **471**, 200 (2011).

[29] A. Bermudez, T. Schaetz, and D. Porras, Phys. Rev. Lett. **107**, 150501 (2011); New J. Phys. **14**, 053049 (2012).

[30] A. Bermudez, T. Schaetz, and M. B. Plenio, Phys. Rev. Lett. **110**, 110502 (2013).

[31] L. Deslauriers, S. Olmschenk, D. Stick, W. K. Hensinger, J. Sterk, and C. Monroe, Phys. Rev. Lett. **97**, 103007 (2006); D. T. C. Allcock, T. P. Harty, H. A. Janacek, N. M. Linke, C. J. Ballance, A. M. Steane, D. M. Lucas, R. L. Jarecki, Jr., S. D. Habermehl, M. G. Blain, D. Stick, and D. L. Moehring, App. Phys. B **107**, 913 (2011); N. Daniilidis, S. Gerber, G. Bolloten, M. Ramm, A. Ransford, E. Ulin-Avila, I. Talukdar, and H. Häffner, Phys. Rev. B **89**, 245435 (2014); M. Brownnutt, M. Kumph, P. Rabl, and R. Blatt, Rev. Mod. Phys. **87**, 1419 (2015).

[32] P. Schindler, D. J. Gorman, N. Daniilidis, and H. Häffner, Phys. Rev. A **92**, 013414 (2015).

[33] C. Schneider, M. Enderlein, T. Huber, and T. Schaetz, Nat. Photonics **4**, 772 (2010); T. Huber, A. Lambrecht, J. Schmidt, L. Karpa, and T. Schaetz, Nat. Comm. **5**, 5587 (2014).

[34] M. Müller, L. Liang, I. Lesanovsky, and P. Zoller, New J. Phys. **10**, 093009 (2008); T. Feldker, P. Bachor, M. Stappel, D. Kolbe, R. Gerritsma, J. Walz, and F. Schmidt-Kaler, Phys. Rev. Lett. **115**, 173001 (2015).